Contents lists available at ScienceDirect

Journal of Hazardous Materials

Synthesis and characterization of Zr^{4+}, La^{3+} and Ce^{3+} doped mesoporous TiO_2: Evaluation of their photocatalytic activity

L. Kumaresan[a], A. Prabhu[a], M. Palanichamy[a], E. Arumugam[b], V. Murugesan[a],*

[a] *Department of Chemistry, Anna University, Chennai 600 025, India*
[b] *Structural Engineering Division, Anna University, Chennai 600 025, India*

ARTICLE INFO

ABSTRACT

Sol–gel method was used to synthesize Zr^{4+}, La^{3+} and Ce^{3+} doped mesoporous TiO_2 materials with different weight percentage (0.5, 1.0, 2.0 and 3.0 wt%) using triblock copolymer as the structure directing template in ethanol/water medium. Characterization revealed the isomorphic substitution of Zr^{4+} ion into the lattice of TiO_2, and surface binding nature of La^{3+} and Ce^{3+} ions on mesoporous TiO_2. Microscopic examination confirmed the surface adsorption of foreign ion which could alter the particle morphology. The size of the particles was less than 20 nm. Photocatalytic activity of metal ions doped mesoporous TiO_2 was evaluated using aqueous alachlor as a model pollutant. It was found that 1 wt% Ce^{3+} doped mesoporous TiO_2 exhibited higher activity than pure and other metal ions doped mesoporous TiO_2. The change of oxidation state of Ce^{3+} is suggested to be the cause for enhanced photocatalytic activity.

© 2010 Elsevier B.V. All rights reserved.

1. Introduction

Semiconductor mediated photocatalytic oxidation offers potentially facile and cheap method for removing organic pollutants from wastewater. Removal of organic compounds in water and wastewater using photocatalytic oxidation technique is an interesting and important area of research for the past 20 years [1–3]. Among the several semiconductors employed for the degradation of organic pollutants, TiO_2 has proven to be a versatile catalyst [4]. The excellent stability coupled with low cost has made TiO_2 as a benchmark catalyst in semiconductor photocatalysis. However, the existing technology has not been successfully commercialized mainly because of the low quantum efficiency of TiO_2, which is due to very fast recombination of photogenerated electron–hole pairs. In order to improve the photocatalytic activity of TiO_2, several modification methods have been developed.

Mesoporous TiO_2 with large surface area will provide a highly active photocatalytic material, and several preparative approaches utilizing supramolecular templating mechanism have been reported for the preparation of mesoporous TiO_2 [5,6]. Mesoporous TiO_2 was first prepared using phosphate surfactant by a modified sol–gel process [7]. However, the product was found to be impure TiO_2 because a significant amount of phosphorous

remained in these materials and they underwent partial collapse of mesostructure during template removal by calcination. Yang et al. [8] prepared mesoporous TiO_2 using amphiphilic poly(alkylene oxide) block copolymers as structure-directing agent and titanium tetrachloride as the precursor in non-aqueous medium. Metal ion doping is an effective method to improve the properties of TiO_2 by modifying their microstructure and phase composition. There are reports on transition and rare earth metal ions as a dopant in TiO_2 to enhance the photocatalytic performance of TiO_2 [9,10]. The presence of dopant ions in TiO_2 structure caused significant absorption shift to the visible region compared to pure TiO_2 [11]. The doping of transition metal ions led to change of electronic environment of Ti^{4+} and zeta potential charge of the catalyst [12].

Zirconium ion doping possibly suppresses the recombination of electrons and holes by trapping [13]. Wang et al. [14] reported that incorporation of Zr^{4+} ion into TiO_2 led to small grain size, high surface area, large lattice deformation and formation of capture traps, all of which contribute to higher separation efficiency of the photogenerated carriers. The improved photocatalytic performance of Zr^{4+} doped TiO_2 is attributed to the strong reduction potential of the photogenerated electrons, resulting from the elevation of conduction band [15]. Venkatachalam et al. [16] reported that doping of Zr^{4+} in nano TiO_2 decreased the particle size and enhanced the adsorption of 4-chlorophenol on the catalyst surface.

Lanthanide ions are known for their ability to form complexes with various Lewis bases (e.g., amines, aldehydes, alcohols, thiols, etc.) by the interaction of functional groups with f-orbitals of lan-

* Corresponding author. Tel.: +91 44 22358645; fax: +91 44 22200889/22201213.
E-mail address: v_murugu@hotmail.com (V. Murugesan).

thanides [17]. In addition, incorporation of lanthanide ions on TiO_2 could provide not only a mean to concentrate the organic pollutants on the semiconductor surface but also stabilize the mesostructure and provide high surface area, and therefore enhance the photocatalytic activity of TiO_2 [18]. Moreover, lanthanide ion doping thermally stabilized the mesoporous structure and retarded the diminishing of surface area of nanosized TiO_2 at high temperatures. On the other hand, Yuan et al. [19] reported the synthesis of lanthanum and cerium doped mesoporous TiO_2 using crystalline nanoparticles as assembly units and triblock copolymer as template. In addition, Xiao et al. [20] have fabricated cerium doped TiO_2 nanoparticles with anatase mesostructure using cetyltrimethylammonium bromide (CTAB) as the structure directing and pore forming agent. Doping of cerium or lanthanum at higher concentration not only improved the thermal stability of hexagonal mesostructure but also restrained the phase transformation. They also reported enhanced growth of crystalline anatase nanoparticles. Moreover, doping of metal ion into mesoporous TiO_2 framework may provide more active sites on the surface of the channel and can add acidity, leading to different physico- chemical properties as well as improved catalytic behavior.

Herbicides are toxic to many organisms and exhibit low solubility in water [21]. Alachlor (2-chloro-2′,6′-diethyl-N-(methoxymethyl)acetanilide) is widely used as a pre- and early post-emergent herbicide in maize field and also as weed control [22]. The maximum contaminant level of alachlor in drinking water was established by the United States Environmental Protection Agency (USEPA) as 2 mg/L [23]. Alachlor causes cancer in laboratory animals and it is classified as group B2 carcinogen by USEPA [24]. In addition, alachlor has toxic and genotoxic effects and can also contribute to infertility [25,26]. Even though pesticides are indispensable in modern civilization, society is aware of their potential toxicity to humans and animals. So the presence of their residues in water and wastewater is a potential hazard to both humans and environment. The removal of pesticides from wastewater effluent is now the subject of considerable concern and has attracted many researchers in the recent years. Since alachlor is very toxic, conventional biological remediation processes are not suitable to remove it from contaminated water, and therefore suitable alternative treatment method is required. Ozonation, photolysis and photocatalysis, photo-Fenton degradation of alachlor in wastewater have been reported [27–29]. Since mesoporous materials possess high surface area, they may be expected to exhibit high photocatalytic activity. In addition, the effect of metal dopant in mesoporous TiO_2 band gap excitation of electron has not been discussed enough in the previous reports. In this article, synthesis of Zr^{4+}, La^{3+} and Ce^{3+} doped mesoporous TiO_2 with different weight percentage using triblock copolymer (Pluronic P123) as the structure directing template in ethanol–water solvent mixture by sol–gel method and characterization of the materials are presented. In addition, the photocatalytic activity of these metal ions doped TiO_2 in the degradation of alachlor in aqueous medium is also evaluated.

2. Materials and methods

2.1. Materials

Titanium(IV) isopropoxide, zirconium(IV) oxynitrate, lanthanum(III) nitrate hexahydrate and cerium(III) nitrate hexahydrate were used as the sources for Ti^{4+}, Zr^{4+}, La^{3+} and Ce^{3+} respectively. Triblock copolymer, poly(ethylene glycol)-block–poly(propylene glycol)-block–poly(ethylene glycol) (Pluronic P123, molecular weight = 5800, $EO_{20}PO_{70}EO_{20}$; Aldrich) was used as the structure directing template. All other reagents (Merck) were used as received without further purification.

2.2. Synthesis of pure and metal doped mesoporous TiO_2

Pure mesoporous TiO_2 was synthesized using soft-template approach with triblock copolymer as the structure directing agent by sol–gel method. Ethanol was used as the co-solute and titanium(IV) isopropoxide was used as the source for Ti^{4+} in the preparation. The gel composition of the synthesis with ethanol as co-solute was: 1 Ti(OiPr)$_4$:50 EtOH:0.00017 P123:18 H_2O. The typical synthesis procedure is as detailed below: triblock copolymer (1 g) was added to ethanol (30 mL). After stirring for 4 h, a clear solution was obtained. Titanium(IV) isopropoxide (3.0 mL) was added to the clear solution and stirred for 2 h at room temperature. Then, water (18 mL) was added to the mixture and stirred continuously for 24 h at room temperature. Subsequently, the resulting mixture was kept in dark overnight for nucleation. The synthesis was carried out in a closed polypropylene bottle. The precipitated product was centrifuged in order to remove the template present in the solution of ethanol–water mixture. The solid product was dried and ground to get fine powder. This material was calcined at 400 °C for 5 h under N_2 atmosphere to remove the occluded template. The synthesized mesoporous TiO_2 material was designated as pure M·TiO_2.

The above procedure was adopted for the preparation of zirconium, lanthanum and cerium doped mesoporous TiO_2 with different (0.5, 1.0, 2.0 and 3.0) wt% by co-precipitation method. After the addition of water under vigorous stirring, stoichiometric amount of the respective metal nitrate was added to the mixture to obtain the required concentration.

2.3. Catalyst characterization

The X-ray diffraction (XRD) patterns of metal doped mesoporous TiO_2 were recorded on a PANalytical X'Pert Pro X-ray diffractometer using CuKα radiation as the X-ray source. The diffractograms were recorded in the 2θ range 5–80° in steps of 0.02° with a count time of 20 s at each point. The average particle size was determined from the broadening of the diffraction peak using the Scherrer formula, $D = K\lambda/\beta \cos\theta$, where D is the average particle size (nm), K is the Scherrer constant, λ is the wavelength of the X-ray source, β is the full width at half-maximum and θ is the Bragg's angle. X-ray photoelectron spectra were recorded on a VG Microtech and MT 500/L using MoKα radiation as the X-ray source for excitation. The data were collected at room temperature, and the operating pressure in the analysis chamber was kept below 10^{-9} Torr. Transmission electron microscopic (TEM) images were recorded using a JEOL TEM-3010 electron microscope operated at an accelerating voltage of 300 keV. Scanning electron microscopic (SEM) pictures were recorded using a scanning electron microscope (HITACHI COM-S-4200) operated at an accelerating voltage of 16 kV. The surface area of the catalysts was measured with Belsorb mini II sorption analyzer using nitrogen as the sorbent at 77 K. Prior to analysis, the samples were degassed for 3 h at 250 °C under vacuum (10^{-5} mbar) in the degas port of the adsorption analyzer. FT-IR spectra were recorded using a FT-IR spectrometer (Nicolet Avator 360). DRS UV–vis spectra of the synthesized materials were recorded in the scan range 210–900 nm using UV–vis spectrophotometer (Shimadzu model 2450) equipped with an integrating sphere and $BaSO_4$ was used as the reference.

2.4. Photocatalytic degradation studies and analysis

Photocatalytic degradation of alachlor was performed in aqueous medium in a slurry batch reactor. A cylindrical photochemical reactor of 30 cm × 2 cm (height × diameter), with a water circulation arrangement to maintain the temperature in the range 25–30 °C, was used in all the experiments. UV irradiation was

carried out using 8×8 W low pressure mercury lamps built into a lamp housing with polished anodized aluminium reflectors placed 12 cm away from the reactor. These lamps emit predominantly UV radiation at a wavelength of 254 nm and another 8 lamps were arranged alternatively to emit UV radiation at a wavelength of 365 nm. The reactor set-up was covered with aluminium foil followed by a black cloth to prevent UV light leakage.

Alachlor stock solution containing 200 mg L^{-1} was prepared in triple distilled water and diluted to the required concentration. In a typical procedure, 100 mg of the catalyst was added to 100 mL alachlor solution of 40 mg L^{-1} and the resultant slurry was stirred for 30 min to attain equilibrium. It was then irradiated with UV light of either 254 or 365 nm with continuous purging of air free from CO_2. Aliquots (5 mL) were withdrawn at specific time intervals, diluted to 10 mL using triple distilled water and analyzed after centrifugation followed by filtration with 0.2 μm membrane to remove the catalyst particles. The extent of degradation and formation of intermediates were monitored using a high performance liquid chromatograph (HPLC; Shimadzu, LC-20 vp prominence pump and SPD-20A UV–vis detector adjustable to 210 and 270 nm with reverse-phase ODS column). The mobile phase in the HPLC was composed of acetonitrile and triple distilled water (70:30 (v/v)). The extent of mineralization of alachlor was followed using a total organic carbon analyzer (TOC; Shimadzu TOC-V CPN).

3. Results and discussion

3.1. XRD

The XRD patterns of pure and Zr^{4+} doped M·TiO$_2$ are presented in Fig. 1. The patterns are comparable to anatase form of TiO$_2$ (JCPDS, file No. 21-1272). The patterns corresponding to Zr^{4+} doped M·TiO$_2$ materials are less intense than pure M·TiO$_2$. This revealed that the crystalline nature of Zr^{4+} doped TiO$_2$ is lower than pure M·TiO$_2$. The peaks at 25.48°, 37.94°, 48.10° (2θ) corresponding to pure M·TiO$_2$ are shifted for Zr^{4+} doped M·TiO$_2$. Since the ionic radius of Zr^{4+} (0.720 Å) is close to Ti^{4+} (0.680 Å), Zr^{4+} ions can substitute the lattice Ti^{4+} ions or incorporate interstitially into the lattice of TiO$_2$ [16,30]. Moreover, both titanium and zirconium are tetravalent; similar surface perfection/imperfection is expected due to defective –OH groups. FT-IR spectral analysis, discussed below, illustrates that M·TiO$_2$ possesses more defective –OH groups than Zr^{4+} doped M·TiO$_2$. Though Zr^{4+} doped M·TiO$_2$ carries less number of defective –OH groups, their intensity in the XRD patterns is lower than pure M·TiO$_2$. Zirconium may be planted on the surface as well as in the bulk of TiO$_2$ crystal in Zr^{4+} doped M·TiO$_2$. Surface planting of zirconium can facilitate reduction of defective –OH groups whereas bulk planting can lead to lattice distortion. If surface planting of Zr^{4+} occurred during synthesis, it could be expected that same level of defective –OH groups may be present as that of M·TiO$_2$. But FT-IR spectra revealed fewer number of defective –OH groups. Hence the reduction in the number of surface –OH groups may be due to reaction between free formed Zr(OH)$_4$ and already available defective –OH groups during calcination.

The XRD patterns of pure and La^{3+} doped M·TiO$_2$ are shown in Fig. 1. The patterns are comparable to anatase form of TiO$_2$ (JCPDS, file No. 21-1272). Separate crystallization of La$_2$O$_3$ is precluded during synthesis. La^{3+} may be incorporated either in the lattice of TiO$_2$ or crystallized as tiny particles of very small dimension below the detectability limit of XRD. Incorporation of La^{3+} in the lattice of TiO$_2$ is confirmed by the shift in the 2θ values of the patterns of all La^{3+} doped M·TiO$_2$. The 2θ values of different wt% La^{3+} doped M·TiO$_2$ (25.35°, 25.38°, 25.4° and 25.34°) corresponding to the patterns of
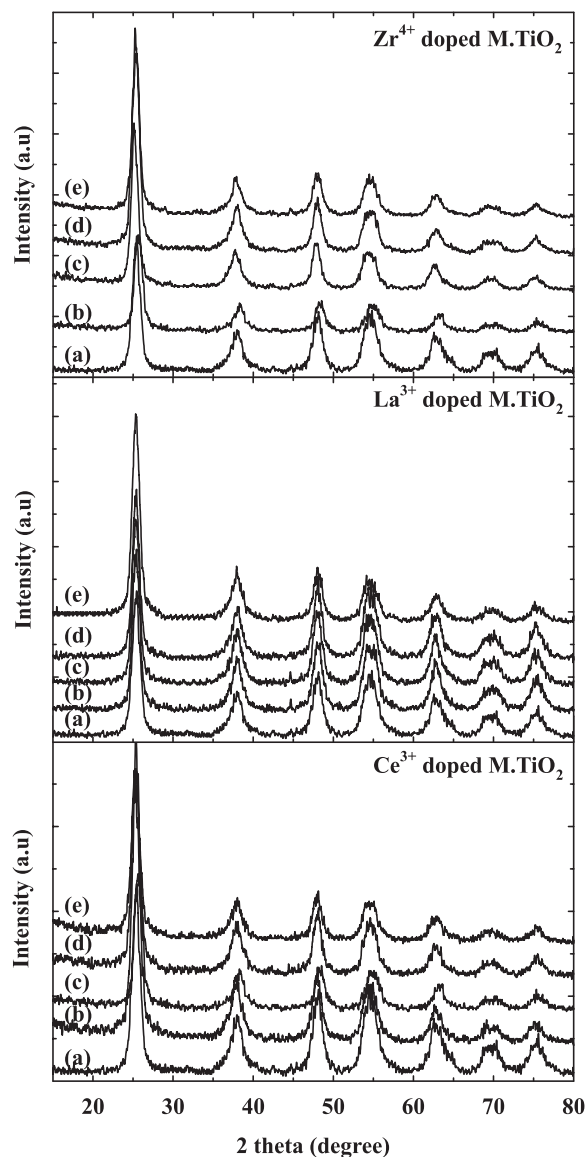

Fig. 1. XRD patterns of Zr^{4+}, La^{3+} and Ce^{3+} doped M·TiO$_2$ with different wt% (a) pure M·TiO$_2$, (b) 0.5 wt%, (c) 1.0 wt%, (d) 2.0 wt% and (e) 3.0 wt%.

(1 0 1) are shifted from 25.48° (2θ) of pure M·TiO$_2$. Since the ionic size of Ti^{4+} (0.680 Å) is not matching with that of La^{3+} (1.150 Å), incorporation of La^{3+} in the inner portion of crystal lattice may not be possible. Moreover, the charge of La^{3+} is one unit less than Ti^{4+} and hence placing La^{3+} in the bulk portion of TiO$_2$ crystal is not allowed. Therefore, the most appropriate place for positioning La^{3+} is the outer surface of TiO$_2$ crystal [31]. The entry of every La^{3+} on the surface creates less number of defective –OH groups on the surface due to covalent bond formation between La^{3+} and M·TiO$_2$. This is confirmed from FT-IR spectral analysis discussed below. Based on the FT-IR spectra and also the intensity of XRD patterns, it is evident that La^{3+} is planted mainly on the external surface.

The XRD patterns of pure and Ce^{3+} doped M·TiO$_2$ are presented in Fig. 1. The intensity of the patterns for Ce^{3+} doped M·TiO$_2$ is slightly decreased for 0.5, 1.0 and 2.0 wt% but largely decreased for 3.0 wt% Ce^{3+} doped M·TiO$_2$ compared to pure M·TiO$_2$. Hence like La^{3+}, Ce^{3+} may be covalently bound to the surface, without being planted in the bulk of TiO$_2$ lattice. There are chances to form oxides of Zr^{4+}, La^{3+} and Ce^{3+} in the corresponding metal doped M·TiO$_2$ at high doping level. But the size of the oxides is small and hence separate patterns for them are not observed in the XRD. Based on the

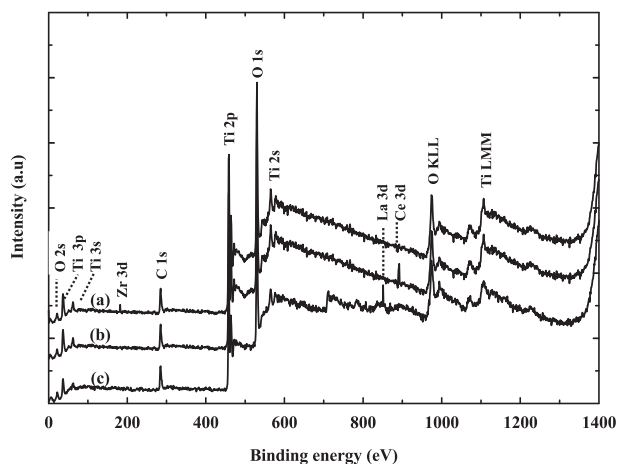**Fig. 2.** XPS spectra of 1.0 wt% metal doped $M \cdot TiO_2$ (a) Zr^{4+} doped $M \cdot TiO_2$, (b) Ce^{3+} doped $M \cdot TiO_2$ and (c) La^{3+} doped $M \cdot TiO_2$.

XRD data, the crystallite size of the metal doped $M \cdot TiO_2$ is calculated using the Scherer equation and it is found to vary from 10 to 15 nm.

3.2. XPS

The XPS spectra of 1 wt% Zr^{4+}, La^{3+} and Ce^{3+} doped $M \cdot TiO_2$ are shown in Fig. 2 The electron subshell (core shell) corresponding to each peak is indicated for each element in the respective spectrum. The binding energies of the level match with those reported in the literature [32–34]. Ti 2p binding energy for all metal doped $M \cdot TiO_2$ is approximately equal to 458.0 eV ($2p_{3/2}$) and 464.0 eV ($2p_{1/2}$) corresponding to Ti^{4+} in tetragonal structure [35–37]. A dominant peak at 530.1 eV, characteristic of metallic oxides, arises from the overlapping contribution of oxygen from TiO_2 and M–O–Ti compounds, among which oxygen from TiO_2 is the primary contributor. The O 1s peak at 531.2 eV is attributed to the hydroxyl group [38].

The Zr 3d spectrum exhibits two peaks with binding energy values of 181.7 and 185.2 eV for Zr $3d_{5/2}$ and Zr $3d_{3/2}$ respectively, as shown in Fig. 3. This is consistent with the values reported in the literature [39]. These results reveal that Zr^{4+} ions are substituted for Ti^{4+} in the TiO_2 lattice. The La 3d spectrum (Fig. 3.) shows peaks with binding energy values of 835, 844 and 852 eV. From the results of La 3d spectrum, it is suggested that lanthanum exists in +3 state in La^{3+} doped $M \cdot TiO_2$. Furthermore, compared to the standard XPS energy peak location of La 3d in La_2O_3, the peak for La 3d spectrum in La^{3+} doped $M \cdot TiO_2$ exhibits a slight chemical shift to low binding energy. This is ascribed to the variation of La^{3+} chemical surroundings and the difference in the distance between lanthanum and oxygen compared with pure La_2O_3 [40,41]. Similarly Ce 3d spectrum of Ce^{3+} doped $M \cdot TiO_2$ is shown in Fig. 3. The presence of Ce $3d_{5/2}$ and Ce $3d_{3/2}$, with binding energy values of 873 and 895 eV respectively, is clearly seen in the spectrum [42]. Hence, as a result of doping, there may not be any change in the oxidation state of the ions.
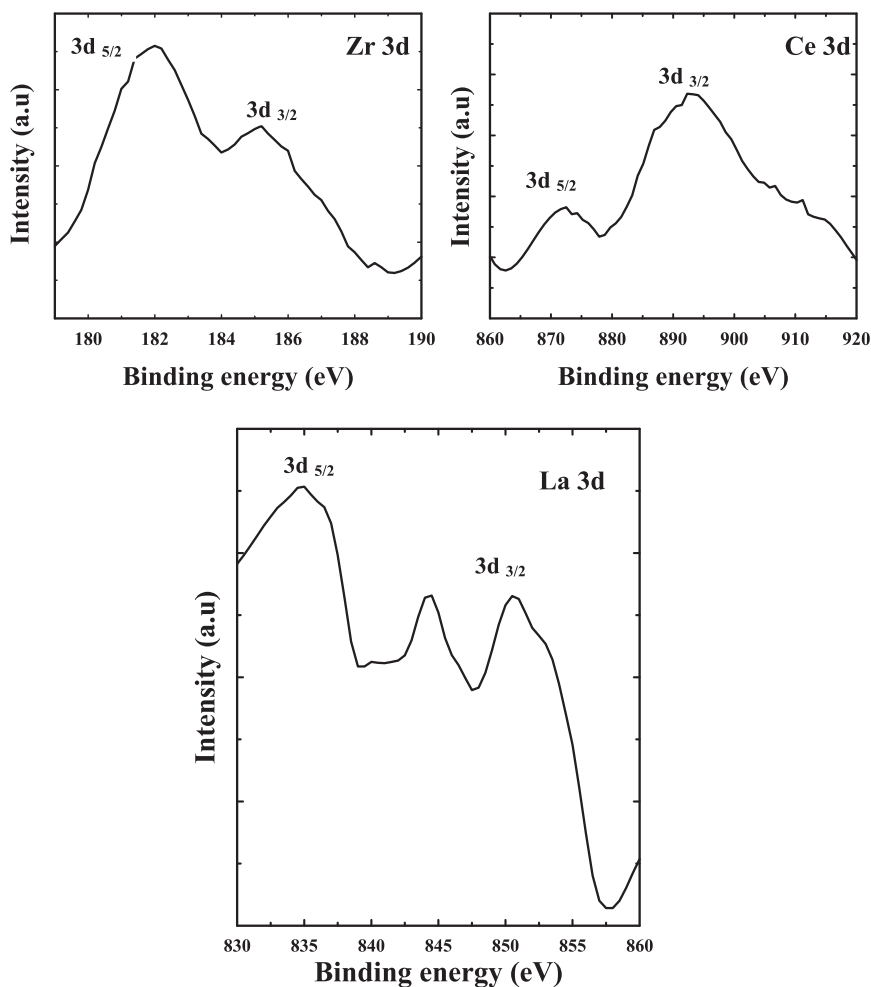

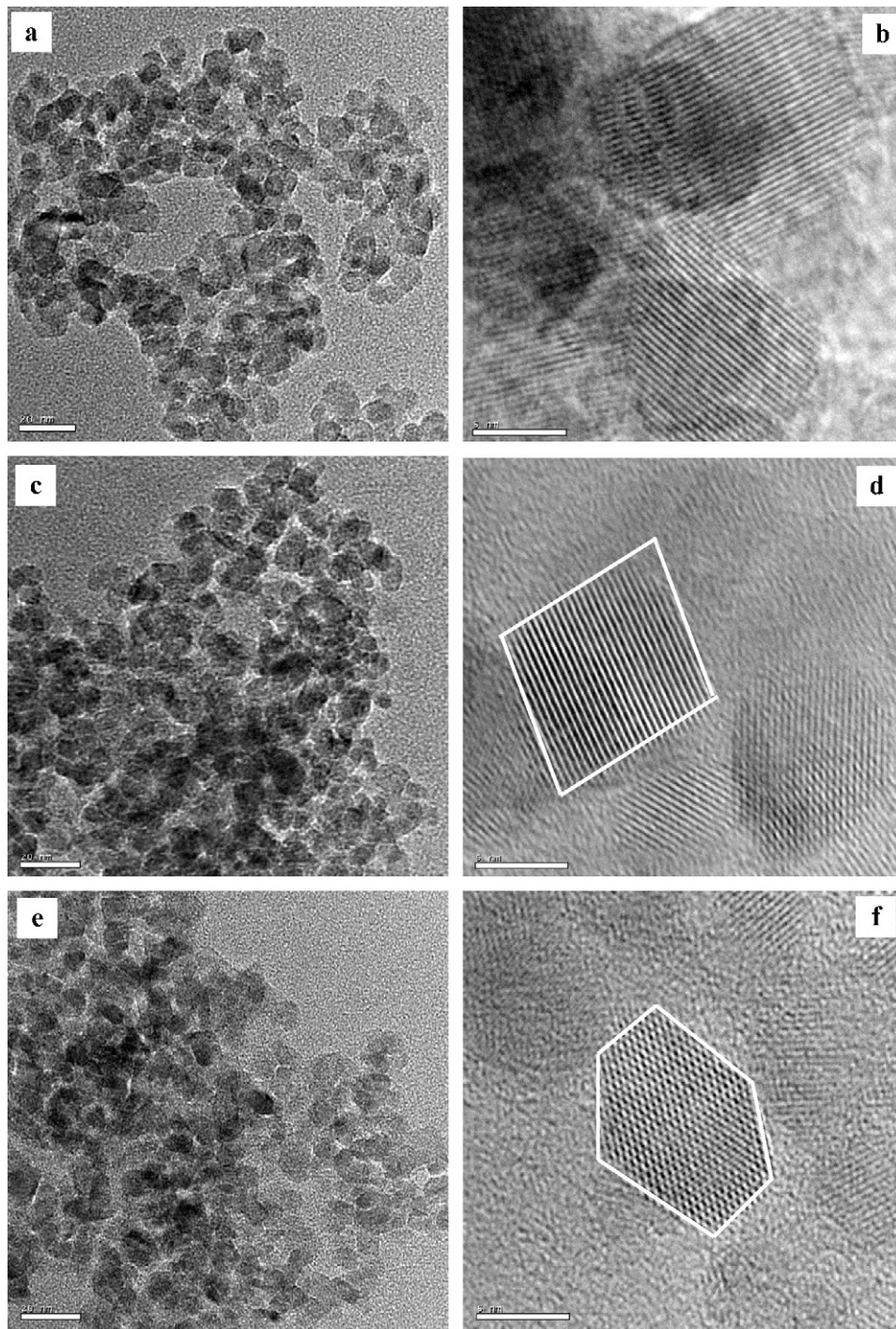**Fig. 3.** 3d XPS spectra of 1 wt% Zr^{4+}, La^{3+} and Ce^{4+} doped $M \cdot TiO_2$.

Fig. 4. TEM images of (a) 1 wt% Zr^{4+} doped $M \cdot TiO_2$, (b) magnified image of 1 wt% Zr^{4+} doped $M \cdot TiO_2$, (c) 1 wt% La^{3+} doped $M \cdot TiO_2$, (d) magnified image of 1 wt% La^{3+} doped $M \cdot TiO_2$, (e) 1 wt% Ce^{3+} doped $M \cdot TiO_2$ and (f) magnified image of 1 wt% Ce^{3+} doped $M \cdot TiO_2$.

3.3. TEM

The TEM images of 1.0 wt% Zr^{4+} doped $M \cdot TiO_2$ are shown in Fig. 4a and b. The particles are roughly spherical in shape with narrow size distribution. The presence of macro voids and agglomeration of the particles are clearly seen. Based on the morphology, it is difficult to discern the particles of zirconia. Hence zirconium may be spread over the entire solid matrix as discussed in XRD. Based on the scale provided, the size of all particles is less than 20 nm. The TEM images of La^{3+} doped $M \cdot TiO_2$ are shown in Fig. 4c and d.

It is very much agglomerated but does not show more voids unlike Zr^{4+} doped $M \cdot TiO_2$. The image of single particle shows a distorted square like morphology as shown in Fig. 4d. The particle size is varying in the range between 5 and 10 nm. TEM images of 1.0 wt% Ce^{3+} doped $M \cdot TiO_2$ are shown in Fig. 4e and f. These images exhibit the same characteristics as that of Zr^{4+} doped $M \cdot TiO_2$. Like La^{3+} doped $M \cdot TiO_2$, Ce^{3+} doped $M \cdot TiO_2$ is also very much agglomerated. The particles appear nearly uniform in size and all of them have size less than 20 nm. The TEM image of a single particle exhibits hexagonal structural arrangement as shown in Fig. 4f.
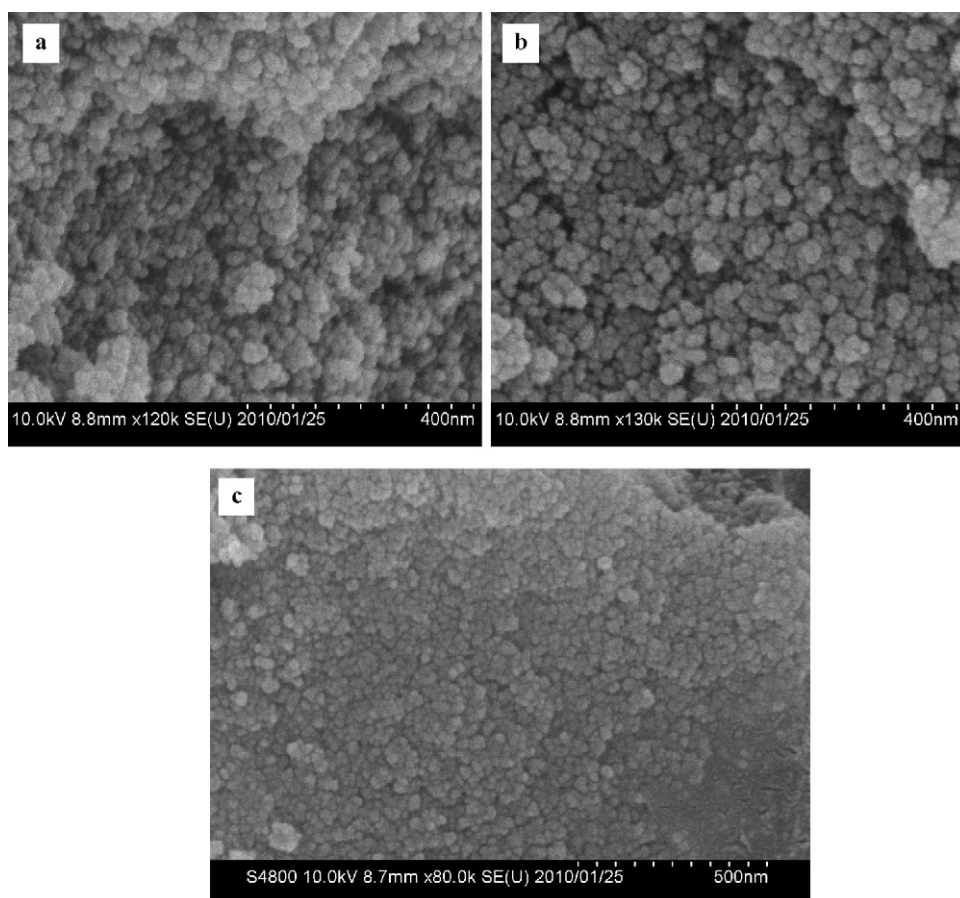
Fig. 5. SEM images of (a) 1.0 wt% Zr^{4+} doped $M \cdot TiO_2$, (b) 1.0 wt% La^{3+} doped $M \cdot TiO_2$ and (c) 1.0 wt% Ce^{3+} doped $M \cdot TiO_2$.

The metal ions seem to control the morphology of particles. Although surface adsorption of foreign metal ions could alter the particle morphology, the medium may also play a significant role in controlling the morphology. Although both trivalent metal ions undergo hydrolysis to form $M(OH)_3$, $M(OH)_2^+$, MO^+, etc. ($M = La^{3+}$ or Ce^{3+}), their concentration may differ for both La^{3+} and Ce^{3+}. As the species are adsorbed on the surface of growing crystals, both metal ions cannot give crystals of similar morphology because of different level of adsorption of such species.

3.4. SEM

The SEM image of 1.0 wt% Zr^{4+} doped $M \cdot TiO_2$ is shown in Fig. 5a. High degree of agglomeration is clearly evident and all of them exhibit similar morphology without any evidence for separate morphology for ZrO_2. This observation is similar to TEM image. Thus TEM and SEM images are clear evidence for complete dispersion of Zr^{4+} on TiO_2 particle.

SEM images of 1.0 wt% La^{3+} and Ce^{3+} doped $M \cdot TiO_2$ are shown in Fig. 5b and c respectively. The morphology of particles is roughly spherical. Separate crystalline particles of lanthanum and cerium oxides are not seen similar to Zr^{4+} doped $M \cdot TiO_2$. Hence La^{3+} and Ce^{3+} ions are well dispersed on TiO_2 particles. Though the particles are nearly the same size as predicted by TEM, the aggregates exhibit varying sizes. Single aggregate is not advantageous, whereas highly dispersed aggregates are significant for photocatalysis. Such highly dispersed aggregates can adsorb even bulky pollutants and do not hinder light penetration like bulk aggregates. Although formation of such dispersed aggregates was not observed during synthesis, such formation is important in photocatalysis.

3.5. Nitrogen sorption analysis

The N_2 adsorption isotherms of pure and Zr^{4+} doped $M \cdot TiO_2$ with different wt% (0.5, 1.0 and 2.0) are shown in Fig. 6. The pure $M \cdot TiO_2$ exhibits type IV adsorption isotherm with the characteristic hysteresis loop for its mesoporous void [43]. The major pores appear with uniform dimension, as the portion corresponding to pore condensation of nitrogen shows a smooth increase. As the curve due to multilayer formation above relative pressure (p/p_0) of 0.9 is not overlapping as that of cooling curve, part of the pore may be larger in dimension than the previous one. The isotherms of Zr^{4+} doped $M \cdot TiO_2$ are almost similar but irregular compared to that of pure $M \cdot TiO_2$. The wide variation in the pore size is clearly evident in all the isotherms. Hence Zr^{4+} incorporation may promote unequal distribution of pore size, and this could be possible if sufficient amount of Zr^{4+} is resting on one particle surface to bind other particles with varying inter particle voids.

The N_2 adsorption isotherms of pure and (0.5, 1.0 and 2.0 wt%) La^{3+} doped $M \cdot TiO_2$ are shown in Fig. 6. The isotherms of La^{3+} doped $M \cdot TiO_2$ exhibit type IV with characteristic hysteresis loop, thus confirming the formation of mesopore similar to pure $M \cdot TiO_2$. The portion corresponding to pore condensation is higher for all La^{3+} doped $M \cdot TiO_2$. Hence surface bound La^{3+} might promote formation of pores of larger volume than pure $M \cdot TiO_2$. The strong Lewis acid properties of La^{3+} may be the cause for the formation of such lengthy pores. Hence similar to zirconium, lanthanum also promotes agglomeration and produces pores with large dimension. N_2 adsorption isotherms of pure and (0.5, 1.0 and 2.0 wt%) Ce^{3+} doped $M \cdot TiO_2$ are depicted in Fig. 6. The isotherms of pure and Ce^{3+} doped $M \cdot TiO_2$ exhibit type IV adsorption with characteristic hysteresis loop, evidently supports the formation of mesopore. But the
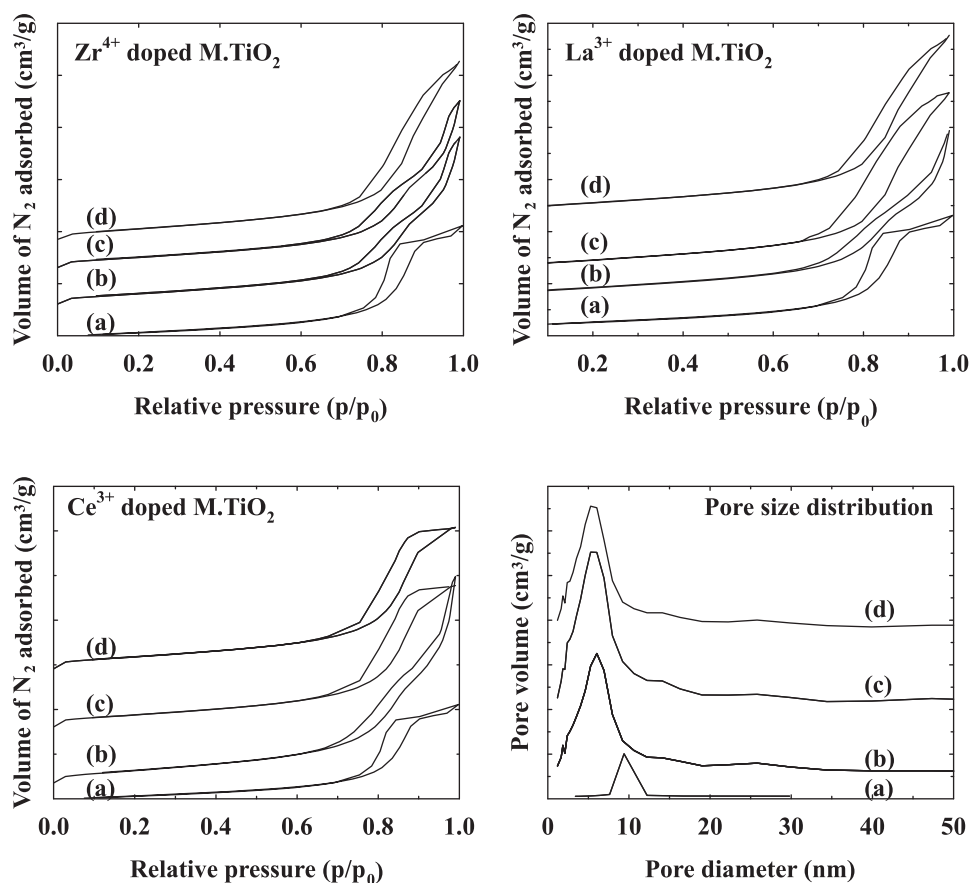
Fig. 6. Nitrogen sorption isotherms of pure and Zr^{4+}, La^{3+} and Ce^{3+} doped M·TiO$_2$ (a) pure, (b) 0.5 wt%, (c) 1.0 wt% and (d) 2.0 wt%; pore size distribution of pure and metal (1.0 wt%) doped M·TiO$_2$ (a) pure M·TiO$_2$, (b) Zr^{4+} doped M·TiO$_2$, (c) La^{3+} doped M·TiO$_2$ and (d) Ce^{3+} doped M·TiO$_2$.

portion corresponding to pore condensation is higher than pure M·TiO$_2$.

The pore size distributions of pure and metal doped M·TiO$_2$ are shown in Fig. 6. The curves for metal doped M·TiO$_2$ are very much broadened compared to pure M·TiO$_2$. In addition, the presence of large pore size greater than 10 nm is also seen in all the metal doped M·TiO$_2$. The formation of such pores may be attributed to the pores created as a result of agglomeration. Hence, surface planted doped metal ion with high Lewis acid property may promote better agglomeration of tiny particles than pure M·TiO$_2$.

3.6. DRS UV–vis

The DRS UV–vis spectra of pure and Zr^{4+} doped M·TiO$_2$ are depicted in Fig. 7. The band gap excitation of Zr^{4+} doped M·TiO$_2$ is shifted towards longer wavelength compared to pure M·TiO$_2$ [44]. Hence Zr^{4+} might covalently interact with TiO$_2$ and modified the band gap of the doped catalysts. Generally shifting of band gap excitation towards longer wavelength is not advantageous for photocatalytic application. But this effect could be compensated by particle agglomeration as evidenced from the absorbance between 400 and 750 nm. There are two absorbance maxima below 400 nm, illustrating formation of two groups of particles with different band gaps. Similarly two absorbance maxima are also observed for pure M·TiO$_2$. Hence crystallization properties of TiO$_2$ may not change by the presence of Zr^{4+} ion and absorbance maximum is also not shifted due to Zr^{4+} doping.

The DRS UV–vis spectra of La^{3+} and Ce^{3+} doped M·TiO$_2$ are also presented in Fig. 7. There are two absorbance bands observed below 400 nm similar to Zr^{4+} doped M·TiO$_2$. The band gap excitation of La^{3+} is nearly equal to pure M·TiO$_2$. But the band gap excitation is shifted to longer wavelength for Ce^{3+} doped M·TiO$_2$. The typical red shift may be attributed to charge-transfer transition between f orbital electrons in the rare earth metal ion and TiO$_2$ conduction or valence band [45,46]. The enhanced red shift shown by Ce^{3+} doped M·TiO$_2$ is a clear additional confirmation for covalent bonding of Ce^{3+} on TiO$_2$ surface. Since Ce^{3+} carries an unpaired electron, new filled energy levels are added to TiO$_2$ in all Ce^{3+} doped M·TiO$_2$. As a result, the band gap is gradually decreased with increase of cerium content. This is the cause for enhanced red shift in the DRS spectra for Ce^{3+} doped M·TiO$_2$. Moreover, the absorbance of Ce^{3+} doped M·TiO$_2$ is increased with increase of cerium content. Hence cerium doping may influence more strongly the band gap of TiO$_2$ particles than lanthanum. They may covalently bind to the surface and facilitate particles agglomeration. Such particles agglomeration leads to formation of giant molecular orbitals, which encompass all the particles together. This may be the cause for absorption in the entire visible region and shift of band gap excitation to longer wavelength. Hence La^{3+} and Ce^{3+} doping may influence the band gap excitation of TiO$_2$ differently. Agglomeration of particles to form giant molecular orbitals is the cause for absorption of light in the visible region.

3.7. FT-IR

The FT-IR spectra of pure and Zr^{4+} doped M·TiO$_2$ are presented in Fig. 8. In all the spectra, the intense broad band between 2700 and 3600 cm^{-1} is assigned to –OH stretching vibration of water. The corresponding bending vibration occurs close to 1630 cm^{-1}. The vibration modes of anatase skeletal O–Ti–O bonds are observed in the range of 500–900 cm^{-1} [47]. At higher energy region, there are peaks between 4000 and 3600 cm^{-1} and they are assigned to defec-
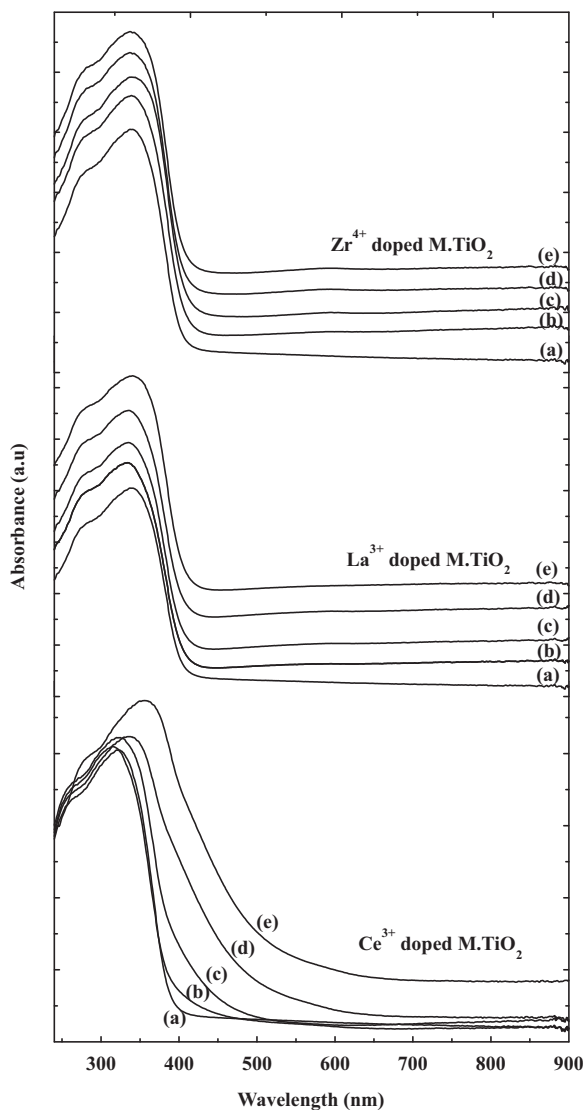
Fig. 7. DRS UV–vis spectra of pure and Zr^{4+}, La^{3+} and Ce^{3+} doped M·TiO$_2$ (a) pure, (b) 0.5 wt%, (c) 1.0 wt%, (d) 2.0 wt% and (e) 3.0 wt%.
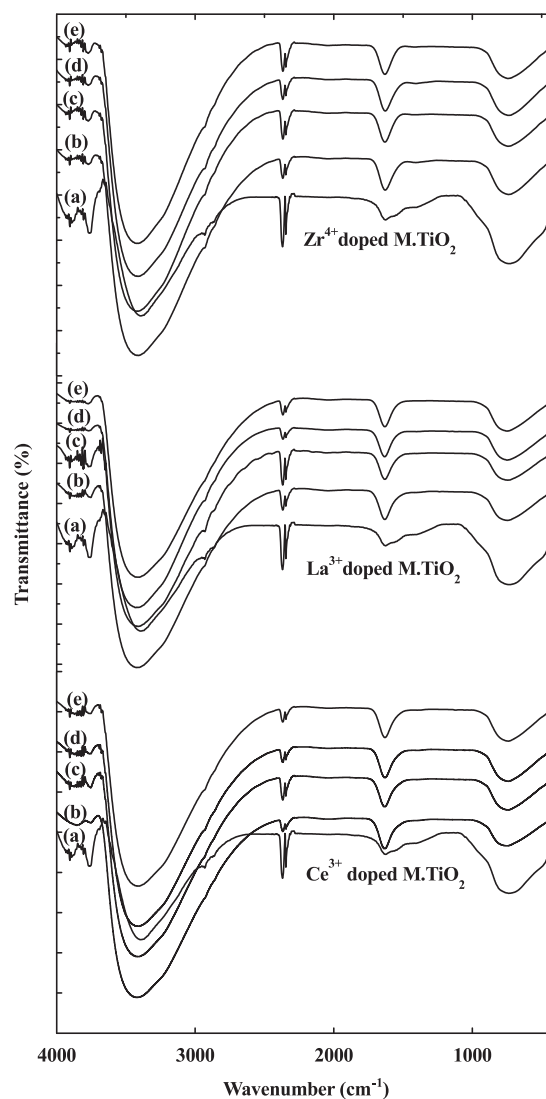
Fig. 8. FT-IR spectra of pure and Zr^{4+}, La^{3+} and Ce^{3+} doped M·TiO$_2$ (a) pure, (b) 0.5 wt%, (c) 1.0 wt%, (d) 2.0 wt% and (e) 3.0 wt%.

tive –OH groups [48]. These peaks are more intense for M·TiO$_2$ than Zr^{4+} doped M·TiO$_2$. Hence Zr^{4+} doping may result in the suppression of defective –OH groups by bonding between Zr^{4+} and –OH group. This is also in accordance with the results of XRD.

The FT-IR spectra of La^{3+} and Ce^{3+} doped M·TiO$_2$ are also shown in Fig. 8. The spectra also display nearly similar features as that of Zr^{4+} doped M·TiO$_2$. The intense peaks due to defective –OH groups decreased as a result of doping. Hence, the surface –OH group may be covalently bound to La^{3+} or Ce^{3+}. Since the ionic size of La^{3+} and Ce^{3+} are higher than Ti^{4+}, the entry of these ions into the bulk TiO$_2$ crystal matrix may not be feasible. But such restriction is not applicable for planting La^{3+} or Ce^{3+} on the surface of TiO$_2$ where these ions can freely interact with defective –OH groups. From the FT-IR spectra, it could be visualized that metal ions are covalently bound to TiO$_2$ particles surface, provided TiO$_2$ carries defective –OH groups on the surface.

3.8. Evaluation of photocatalytic activity of metal doped mesoporous TiO$_2$

The photocatalytic activity of pure and Zr^{4+}, La^{3+} and Ce^{3+} (1 wt%) doped M·TiO$_2$ was evaluated in the degradation of alachlor

in aqueous medium. The progress of the reaction was monitored by measuring TOC at regular intervals. The plot of TOC versus irradiation time is shown in Fig. 9. The pure and metal doped M·TiO$_2$ showed decrease in TOC with increase in irradiation time. The decrease in TOC was much rapid upto 2.5 h beyond which it was slow. Ce^{3+} (1 wt%) doped M·TiO$_2$ showed higher rate of degradation than others. The mineralization was completed at the end of 3.5 h over Ce^{3+} doped M·TiO$_2$ whereas it required 4 h for other metal doped and pure M·TiO$_2$. Ce^{3+} doped M·TiO$_2$ photocatalysts are better than others for mineralization of alachlor. As metal doped M·TiO$_2$ catalysts are found to be better than pure M·TiO$_2$, agglomeration assisted by the metal dopant felicitated excited electron transport from the excited particle. This may be the cause for the enhanced degradation. Since chlorine in alachlor is removed as chloride ion during degradation, monitoring of chloride ion concentration of reaction mixture at regular intervals of irradiation time was also measured to envisage the progress of degradation with 1.0 wt% Ce^{3+} doped M·TiO$_2$. The results are presented in Fig. 9 (inset). The observation of rapid increase in chloride ion concentration up to 2 h and thereafter a steady concentration of chloride ion illustrates the completion of degradation of alachlor. Hence, maximum percentage of degradation of alachlor could be achieved within 2 h.
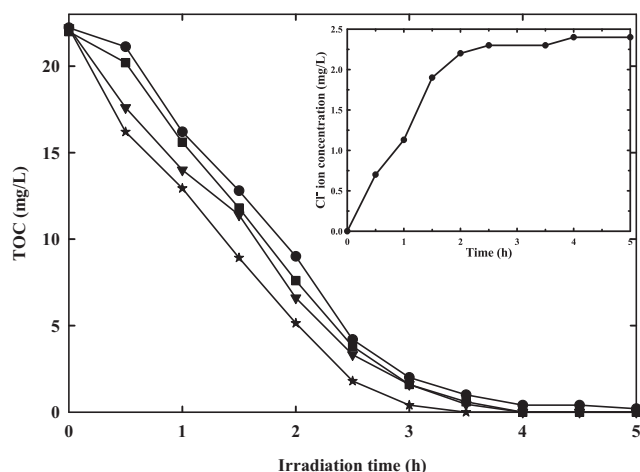
Fig. 9. Photocatalytic mineralization of alachlor at light wavelength 365 nm using pure and metal (1 wt%) doped M·TiO$_2$: (●) pure, (■) Zr^{4+} doped M·TiO$_2$, (▼)La^{3+} doped M·TiO$_2$ and (★) Ce^{3+} doped M·TiO$_2$; the formation chloride ion during the degradation of alachlor using Ce^{3+} doped M·TiO$_2$ (inset).

The decrease in the intensity of the peak (at retention time of 13.0 min) due to degradation of alachlor and appearance of new peaks (at retention time of 10.80 and 19.25 min) due to formation of fragments during photocatalysis were clearly seen in the HPLC chromatograms (figure not included). The complete disappearance of alachlor and its fragments were also evident in HPLC chromatograms. Thus the HPLC chromatograms are evident for degradation of alachlor and therefore the decrease in the TOC value is due to degradation and not due to adsorption.

The rapid decrease in TOC over Ce^{3+} (1.0 wt%) doped M·TiO$_2$ could be explained as follows: Since Ce^{3+} ion can be reduced to unstable Ce^{2+}, the band gap excited electrons could be used to form Ce^{2+}. This act of electron pirating could minimize electron–hole recombination and facilitates generation of hydroxyl radical in the oxidation of water by hole. Such redox properties are possible for cerium and not for other metals. The reduced Ce^{2+} can be oxidized back to Ce^{3+} either by dissolved oxygen or by the hole [49]. Ce^{2+} is not necessarily be oxidized by the hole of the same particle. The formation of agglomerates can rapidly transport band gap excited electrons delocalizing over all the particles of agglomerates. In other words Ce^{3+} ion could be a better electron sink to suppress electron–hole recombination.

4. Conclusion

Zr^{4+}, La^{3+} and Ce^{3+} doped mesoporous TiO$_2$ can be conveniently prepared by sol–gel method involving co-precipitation of titanium and respective metal ion dopant in the presence of triblock copolymer (Pluronic P123) as the structure directing agent. Crystallization of exclusive anatase phase in all three metal ion doped M·TiO$_2$ is evident from XRD patterns. TEM and SEM images revealed agglomeration of particles in all the materials. The entry of Zr^{4+} ion into the lattice of TiO$_2$ and surface binding of La^{3+} and Ce^{3+} on TiO$_2$ are confirmed from XRD. FT-IR spectra also confirmed the surface binding of La^{3+} and Ce^{3+} on TiO$_2$ based on the decrease in the intensity of –OH stretching of TiO$_2$. The photocatalytic activity in the mineralization of alachlor in aqueous solution concluded that Zr^{4+}, La^{3+} and Ce^{3+} doped M·TiO$_2$ are better than pure M·TiO$_2$. As Ce^{3+} doped M·TiO$_2$ showed better activity than other doped M·TiO$_2$, change in the oxidation state of Ce^{3+} is suggested to be the cause for the enhanced activity. It is suggested that Ce^{3+} is reduced to unstable Ce^{2+} state during the mineralization process, but it is not fully established. Oxidation of Ce^{3+} to Ce^{4+} is not useful in the study as

mineralization will be completely lost by this oxidation. This study also provides additional conclusion that doping of TiO$_2$ with metal ion of highly unstable reduced state is better for photocatalytic studies than other metal ions.

References

[1] A.L. Linsebigler, G. Lu, J.T. Yates, Photocatalysis on TiO$_2$ surfaces: principles, mechanisms and selected results, Chem. Rev. 95 (1995) 735–758.
[2] A. Fujishima, T.N. Rao, D.A. Tryk, Titanium dioxide photocatalysis, J. Photochem. Photobiol. C: Photochem. Rev. 1 (2000) 1–21.
[3] S. Malato, J. Blanco, J. Caceres, A.R. Fernandez Alba, A. Aguera, A. Rodriguez, Photocatalytic degradation of water-soluble pesticides by photo-Fenton and TiO$_2$ using solar energy, Catal. Today 76 (2002) 209–220.
[4] S. Malato, F.P. Ibanez, M.I. Maldonado, J. Blanco, W. Gernjak, Decontamination and disinfection of water by solar photocatalysis: recent overview and trends, Catal. Today 147 (2009) 1–59.
[5] J.C. Yu, J. Yu, J. Zhao, Enhanced photocatalytic activity of mesoporous and ordinary TiO$_2$ thin films by sulfuric acid treatment, Appl. Catal. B: Environ. 36 (2002) 31–43.
[6] D.M. Antonelli, J.Y. Ying, Synthesis of hexagonally packed mesoporous TiO$_2$ by a modified sol–gel method, Angew. Chem. Int. Ed. 34 (1995) 2014–2017.
[7] D.M. Antonelli, A. Nakahira, J.Y. Ying, Ligand-assisted liquid crystal templating in mesoporous niobium oxide molecular sieves, Inorg. Chem. 35 (1996) 3126–3136.
[8] P. Yang, D. Zhao, D.I. Margolese, B.F. Fredrickson, B. Chmelka, G.D. Stucky, Hierarchically ordered oxides, Science 282 (1998) 2244–2246.
[9] A.D. Paola, E.G. Lopez, G. Marci, C. Martin, L. Palmisano, V. Rives, A.M. Venezia, Surface characterization of metal ions loaded TiO$_2$ photocatalysts: structure–activity relationship, Appl. Catal. B: Environ. 48 (2004) 223–233.
[10] D. Dana, B. Vlasta, M. Milan, M.A. Malati, Investigations of metal-doped titanium dioxide photocatalysts, Appl. Catal. B: Environ. 37 (2002) 91–105.
[11] P.A. Di, L.E. Garcıa, S. Ikeda, Photocatalytic degradation of organic compounds in aqueous systems by transition metal doped polycrystalline TiO$_2$, Catal. Today 75 (2002) 87–93.
[12] C. Hu, Y.C. Tang, H.X. Tang, Characterization and photocatalytic activity of transition-metal-supported surface bond-conjugated TiO$_2$/SiO$_2$, Catal. Today 90 (2004) 325–330.
[13] S.T. Pantelides, The electronic structure of impurities and other point defects in semiconductors, Rev. Mod. Phys. 50 (1978) 797–858.
[14] Y.M. Wang, S.W. Liu, M.K. Lü, S.F. Wang, F. Gu, X.Z. Gai, X.P. Cui, J. Pan, Preparation and photocatalytic properties of Zr^{4+}-doped TiO$_2$ nanocrystals, J. Mol. Catal. A 215 (2004) 137–142.
[15] B. Gao, T. Mariana, D. Puspitaningrum, T. Lim, Zr-doped TiO$_2$ for enhanced photocatalytic degradation of bisphenol A, Appl. Catal. A: Gen. 375 (2010) 107–115.
[16] N. Venkatachalam, M. Palanichamy, B. Arabindoo, V. Murugesan, Enhanced photocatalytic degradation of 4-chlorophenol by Zr^{4+} doped nano TiO$_2$, J. Mol. Catal. A: Chem. 266 (2007) 158–165.
[17] K.T. Ranjit, I. Willner, S.H. Bossmann, A.M. Braun, Lanthanide oxide doped titanium dioxide photocatalysts: effective photocatalysts for the enhanced degradation of salicylic acid and t-cinnamic acid, J. Catal. 204 (2001) 305–313.
[18] Y. Zhang, H. Zhang, Y. Xu, Y. Wang, Significant effect of lanthanide doping on the texture and properties of nanocrystalline mesoporous TiO$_2$, J. Solid State Chem. 177 (2004) 3490–3498.
[19] S. Yuan, Q. Sheng, J. Zhang, F. Chen, M. Anpo, Q. Zhang, Synthesis of La^{3+} doped mesoporous titania with highly crystallized walls, Microporous Mesoporous Mater. 79 (2005) 93–99.
[20] J. Xiao, T. Peng, R. Li, Z. Peng, C. Yan, Preparation, phase transformation and photocatalytic activities of cerium-doped mesoporous titania nanoparticles, J. Solid State Chem. 179 (2006) 1161–1170.
[21] F. Beltran, B. Acedo, J. Rivas, Use of ozone to remove alachlor from surface water, Bull. Environ. Contamin. Toxicol. 62 (1999) 324–329.
[22] A. Seiler, P. Brenneisen, D.H. Green, Benefits and risks of plant protection products possibilities of protecting drinking water: case atrazine, Water Supply 10 (1992) 31–42.
[23] S.J. Larson, R.J. Gilliom, P.D. Capel, Pesticides in streams of the United States initial results from the National Water Quality Assessment Program, U.S. Geo-

logical Survey Water-Resources Investigations Report 98-4222, U.S. Geological Survey: Sacramento, California, 1999.

[24] E. Charizopoulos, E. Papadopoulou Mourkidou, Occurrence of pesticides in rain of the axios river basin, Greece, Environ. Sci. Technol. 33 (1999) 2363–2368.

[25] O. Osano, W. Admiraala, H.J.C. Klamerc, D. Pastorc, E.A.J. Bleekera, Comparative toxic and genotoxic effects of chloroacetanilides, formamidines and their degradation products on *Vibrio fischeri* and *Chironomus riparius*, Environ. Pollut. 119 (2002) 195–202.

[26] G. Grizard, L. Ouchchane, H. Roddier, C. Artonne, B. Sion, M.P. Vasson, L. Janny, *In vitro* alachlor effects on reactive oxygen species generation, motility patterns and apoptosis markers in human spermatozoa, Reprod. Toxicol. 23 (2007) 55–62.

[27] H.Y. Li, J.H. Qu, H.J. Liu, Decomposition of alachlor by ozonation and its mechanism, J. Environ. Sci. 19 (2007) 769–775.

[28] C.C. Wong, W. Chu, The direct photolysis and photocatalytic degradation of alachlor at different TiO_2 and UV sources, Chemosphere 50 (2003) 981–987.

[29] H. Katsumata, S. Kaneco, T. Suzuki, K. Ohta, Y. Yobiko, Photo-Fenton degradation of alachlor in the presence of citrate solution, J. Photochem. Photobiol. A: Chem. 180 (2006) 38–45.

[30] A.F. Shojaie, M.H. Loghmani, La^{3+} and Zr^{4+} co-doped anatase nano TiO_2 by sol-microwave method, Chem. Eng. J. 157 (2010) 263–269.

[31] F.B. Li, X.Z. Li, M.F. Hou, Photocatalytic degradation of 2-mercaptobenzothiazole in aqueous La^{3+}–TiO_2 suspension for odor control, Appl. Catal. B: Environ. 48 (2004) 185–194.

[32] J. Liqiang, S. Xiaojun, X. Baifu, W. Baiqi, C. Weimin, F. Honggang, The preparation and characterization of La doped TiO_2 nanoparticles and their photocatalytic activity, J. Solid State Chem. 177 (2004) 3375–3382.

[33] E. Beche, P. Charvin, D. Perarnau, S. Abanades, G. Flamant, Ce 3d XPS investigation of cerium oxides and mixed cerium oxide ($Ce_xTi_yO_z$), Surf. Interface Anal. 40 (2008) 264–267.

[34] H. Liu, G. Liu, Q. Zhou, Preparation and characterization of Zr doped TiO_2 nanotube arrays on the titanium sheet and their enhanced photocatalytic activity, J. Solid State Chem. 182 (2009) 3238–3242.

[35] Z.F. Liu, J. Tabora, R.J. Davis, Relationships between microstructure and surface acidity of Ti–Si mixed oxide catalysts, J. Catal. 149 (1994) 117–126.

[36] F.B. Li, X.Z. Li, M.F. Hou, K.W. Cheah, W.C.H. Choy, Enhanced photocatalytic activity of Ce^{3+}–TiO_2 for 2-mercaptobenzothiazole degradation in aqueous suspension for odour control, Appl. Catal. A: Gen. 285 (2005) 181–189.

[37] I. Losito, A. Amorisco, F. Palmisano, P.G. Zambonin, X-ray photoelectron spectroscopy characterization of composite TiO_2–poly(vinylidenefluoride) films synthesised for applications in pesticide photocatalytic degradation, Appl. Surf. Sci. 240 (2005) 180–188.

[38] C. Xie, Z. Xu, Q. Yang, B. Xue, Y. Du, J. Zhang, Enhanced photocatalytic activity of titania–silica mixed oxide prepared via basic hydrolyzation, Mater. Sci. Eng. B 112 (2004) 34–41.

[39] J.C. Yu, J. Lin, R.W.M. Kwok, $Ti_{1-x}Zr_xO_2$ solid solutions for the photocatalytic degradation of acetone in air, J. Phys. Chem. B 102 (1998) 5094–5098.

[40] Q. Chen, D. Jiang, W. Shi, D. Wu, Y. Xu, Visible-light-activated Ce–Si co-doped TiO_2 photocatalyst, Appl. Surf. Sci. 255 (2009) 7918–7924.

[41] E.R. Leite, A.P. Maciel, I.T. Weber, P.N.L. Filho, E. Longo, C.O.P. Santos, A.V.C. Andrade, C.A. Pakoscimas, Y. Maniette, W.H. Schreiner, Development of metal oxide nanoparticles with high stability against particle growth using a metastable solid solution, Adv. Mater. 14 (2002) 905–908.

[42] J. Yang, M. Gao, L. Yang, Y. Zhang, J. Lang, D. Wang, Y. Wang, H. Liu, H. Fan, Low temperature growth and optical properties of Ce-doped ZnO nanorods, Appl. Surf. Sci. 255 (2008) 2646–2650.

[43] K.S.W. Sing, D.H. Everett, R.A.W. Haul, L. Moscou, R.A. Pierotti, J. Rouquerol, T. Siemieniewska, Reporting physisorption data for gas/solid systems with special reference to the determination of surface area and porosity, Pure Appl. Chem. 57 (1985) 603–619.

[44] B. Neppolian, Q. Wang, H. Yamashita, H. Choi, Synthesis and characterization of ZrO_2–TiO_2 binary oxide semiconductor nanoparticles: application and interparticle electron transfer process, Appl. Catal. A: Gen. 333 (2007) 264–271.

[45] A.W. Xu, Y. Gao, H.Q. Liu, The preparation, characterization, and their photocatalytic activities of rare-earth-doped TiO_2 nanoparticles, J. Catal. 207 (2002) 151–157.

[46] Z. Liu, B. Guo, L. Hong, H. Jiang, Preparation and characterization of cerium oxide doped TiO_2 nanoparticles, J. Phys. Chem. Solids 66 (2005) 161–167.

[47] G. Cristallo, E. Roncari, A. Rinaldo, F. Trifiro, Study of anatase–rutile transition phase in monolithic catalyst V_2O_5/TiO_2 and V_2O_5–WO_3/TiO_2, Appl. Catal. A: Gen. 209 (2005) 249–256.

[48] G. Li, L. Li, J.B. Goates, B.F. Woodfield, High purity anatase TiO_2 nanocrystals: near room-temperature synthesis, grain growth kinetics, and surface hydration chemistry, J. Am. Chem. Soc. 127 (2005) 8659–8666.

[49] J. Zhang, L. Xiao, Y. Cong, M. Anpo, Preparation and characterization of multi-functional titanium dioxide photocatalysts, Top. Catal. 47 (2008) 122–130.